The Astrophysical Journal Letters, 861:L23 (7pp), 2018 July 10 https://doi.org/10.3847/2041-8213/aacff5

The Highly Polarized Dusty Emission Core of Cygnus A

Enrique Lopez-Rodriguez[1,2], Robert Antonucci[3], Ranga-Ram Chary[4], and Makoto Kishimoto[5]
[1] SOFIA Science Center, NASA Ames Research Center, Moffett Field, CA 94035, USA; elopezrodriguez@sofia.usra.edu
[2] National Astronomical Observatory of Japan, National Institutes of Natural Sciences (NINS), 2-21-1 Osawa, Mitaka, Tokyo 181-8588, Japan
[3] Department of Physics, University of California in Santa Barbara, Broida Hall, Santa Barbara, CA 93109, USA
[4] IPAC/Caltech, MS314-6, Pasadena, CA 91125, USA
[5] Department of Physics, Kyoto Sangyo University, Motoyama, Kamigamo, Kita-ku, Kyoto, 603-8555, Japan
Received 2018 May 28; revised 2018 June 19; accepted 2018 June 28; published 2018 July 13

Abstract

We report the detection of linearly polarized emission at 53 and 89 μm from the radio-loud active galactic nucleus (AGN) Cygnus A using High-resolution Airborne Wideband Camera-plus (HAWC+) on board the Stratospheric Observatory For Infrared Astronomy (SOFIA). We measure a highly polarized core of 11 $\pm$ 3% and 9 $\pm$ 2% with a position angle (PA) of polarization of 43° $\pm$ 8° and 39° $\pm$ 7° at 53 and 89 μm, respectively. We find (1) a synchrotron-dominated core with a flat spectrum ($+0.21 \pm 0.05$) and a turnover at 543 $\pm$ 120 μm, which implies synchrotron emission is insignificant in the infrared (IR), and (2) a 2–500 μm bump peaking at ~40 μm described by a blackbody component with color temperature of 107 $\pm$ 9 K. The polarized spectral energy distribution (SED) has the same shape as the IR bump of the total flux SED. We observe a change in the PA of polarization of ~20° from 2 to 89 μm, which suggests a change of polarization mechanisms. The ultraviolet, optical, and near-IR (NIR) polarization has been convincingly attributed to scattering by polar dust, consistent with the usual torus scenario, though this scattered component can only be directly observed from the core in the NIR. By contrast, the gradual rotation by ~20° toward the far-IR (FIR), and the near-perfect match between the total and polarized IR bumps, indicate that dust emission from aligned dust grains becomes dominant at 10–100 μm, with a large polarization of 10% at a nearly constant PA. This result suggests that a coherent dusty and magnetic field structure dominates the 10–100 μm emission around the AGN.

Key words: galaxies: active – galaxies: individual (Cygnus A) – galaxies: nuclei – infrared: galaxies – techniques: polarimetric

1. Introduction

Cygnus A ($z = 0.0562$, Stockton et al. 1994, $H_o = 73\,\mathrm{km\,s^{-1}\,Mpc^{-1}}$; $1'' \sim 1$ kpc) is the most studied Faranoff–Riley II (FRII) radio galaxy. This galaxy shows a complex central few kpc (patchy dust lane, dusty ionization cone, and jets), with a heavily extinguished core. Moderate (few arcsec; few kpc) and subarcsecond (few hundred pc) angular resolution observations of the nucleus of Cygnus A have provided unclear dominant physical components. Privon et al. (2012) suggested that star-forming regions in the far-infrared (FIR), a thermal component at near-infrared (NIR) and mid-infrared (MIR) wavelengths, and a synchrotron component at radio wavelengths are the main physical components at scales of few kpc. However, Koljonen et al. (2015) suggested that the core is dominated by a synchrotron component with a turnover in the infrared (IR) wavelength range at scales of a few hundred pc.

Polarimetric techniques provide an alternative approach to study the core and surrounding environments of an active galactic nucleus (AGN). Optical (Tadhunter et al. 1990; Ogle et al. 1997) and ultraviolet (UV; Hurt et al. 1999) polarimetric observations show that the dominant polarization mechanism arises from scattering in the extended cones, while the central few kpc is obscured at these wavelengths. This result is in agreement with the unified model of AGNs (Antonucci 1993; Urry & Padovani 1995). However, due to the kpc-scale dust lane in Cygnus A, and other radio sources, optical and UV observations do not provide significant information about the core due to extinction (i.e., Antonucci & Barvainis 1990). IR and (sub-)mm observations are required to study the core of radio galaxies.

Ramírez et al. (2014) performed 2.05 μm imaging polarimetric observations of 13 FRII radio sources using Near Infrared Camera and Multi-Object Spectrometer/*Hubble Space Telescope* (NICMOS/*HST*) and found a generally high intrinsic polarized (6%–60%) core, and a moderately strong tendency for the position angle (PA) of polarization to be perpendicular to the jet direction. These authors suggested that the dominant polarization mechanism at 2.05 μm arises from dichroic extinction in the core of these radio sources, although other polarization mechanisms could also be present. For Cygnus A, subarcsecond angular resolution 2.0 μm observations using NICMOS/*HST* by Tadhunter et al. (2000) measured a highly polarized (~10% observed, ~28% starlight-corrected) core with a PA of polarization (201° $\pm$ 3°) nearly perpendicular to the radio jet ($\mathrm{P.A._{jet}} \sim 284°$, Sorathia et al. 1996). These results indicate that the 2 μm polarization arises from scattering within the central 375 pc.

Further subarcsecond resolution 10 μm observations using CanariCam on the 10.4 m Gran Telescopio CANARIAS (GTC) by Lopez-Rodriguez et al. (2014) also found a highly polarized (~10%) core within the central 0.″38 (380 pc) with a slight shift in the PA of polarization of ~10° with respect to the 2 μm observations. The change in PA of polarization from 2 to 10 μm indicates that a different polarization mechanism may dominate at longer wavelengths. These authors suggested that the 10 μm polarization arises from a self-absorbed synchrotron component with a turnover at ~34 μm attributed to the pc-scale jet close to the core. The self-absorbed synchrotron component with a break in the IR wavelength range (Privon et al. 2012; Lopez-Rodriguez et al. 2014;

Merlo et al. 2014; Koljonen et al. 2015) implies that the emission arises from a single zone with highly coherent magnetic field in the jet, and with a sharp stop in the production of electrons above the break frequency. Empirically, Antonucci et al. (1990) found that lobe-dominated radio galaxy cores are dominated by self-absorbed synchrotron emission with a break at mm wavelengths. This result shows a jet-dominated core at long wavelengths, while a thermal mechanism dominates the core in the IR. Thus, SED modeling of Cygnus A is in contradiction with the empirical findings in lobe-dominated radio galaxies. Total and polarization flux observations in the FIR and mm are required to disentangle the thermal and non-thermal components in the core of radio-loud galaxies.

We present FIR imaging polarimetric observations of the core of Cygnus A, and the total and polarized nuclear SED from 2 μm to sub-mm wavelengths. We will show that such a combination allows us to disentangle the thermal and non-thermal components in the core of Cygnus A.

2. The FIR Polarimetric Observations

Cygnus A was observed (PI: E. Lopez-Rodriguez, ID: 05_0071) on 20171025/27 using the High-resolution Airborne Wideband Camera-plus (HAWC+; Vaillancourt et al. 2007, Harper et al. 2018) on the 2.5 m Stratospheric Observatory For Infrared Astronomy (SOFIA) telescope. We made observations using the chop-nod polarimetric mode at 53 μm ($\lambda_C = 53$ μm, $\Delta\lambda/\lambda_c = 0.17$ bandwidth) and 89 μm ($\lambda_C = 88.7$ μm, $\Delta\lambda/\lambda_c = 0.19$ bandwidth). HAWC+ polarimetric observations simultaneously measure two orthogonal components of linear polarization arranged in two pairs of arrays of 32 × 40 pixels each, with angular resolution of 2.″55 and 4.″02 per pixel at 53 and 89 μm, respectively. The beam size has been estimated to be 4.″85 and 7.″80 at 53 and 89 μm, respectively.

In both bands, we performed observations in a four-dither pattern with an offset of three pixels, where four halfwave plate PAs were taken in each dither position. We used nod times of 35 s and 40 s at 53 and 89 μm, respectively, with a chop frequency of 10.2 Hz, chop-amplitude of 90″, and chop-angle of 90° with respect to the short axis of the array. Based on the morphology of the source in the *Herschel* observations (Section 3.1), the chop-throw and chop-angle configuration do not result in any significant flux contribution from the radio sources and/or diffuse emission from the background. At 53 μm, six and three dither sets were taken the first and the second night of observations, respectively. Several dither sets were acquired with chop-throws of 180″, providing a slightly elongated image due to misalignments by the chop-nod of SOFIA. To minimize potential polarization contamination due to misaligned images, we removed these data sets from the analysis. At 89 μm, five dither sets were taken the second night of observations. Final observations provide a total exposure time of 1399 s and 1483 s at 53 and 89 μm, respectively. Data were reduced using the HAWC_DPR PIPELINE v1.3.0beta1 and custom PYTHON routines. The pipeline follows the procedure as described by M. Berthoud et al. (2018, in preparation). Raw data were demodulated, chop-nod and background subtracted, flux calibrated and Stokes parameters estimated with their uncertainties. In order to account for systematic or random uncertainties, we performed a reduced-χ^2 analysis on the polarimetric data. We estimated an excess noise factor of $\sqrt{\chi^2/\chi^2_t} \sim 1.16$, where χ^2_t is the theoretical reduced-χ^2 for a given set of observations. Finally, we inflated the uncertainties of the Stokes parameters such that the final excess noise factor $\sqrt{\chi^2/\chi^2_t} = 1$.

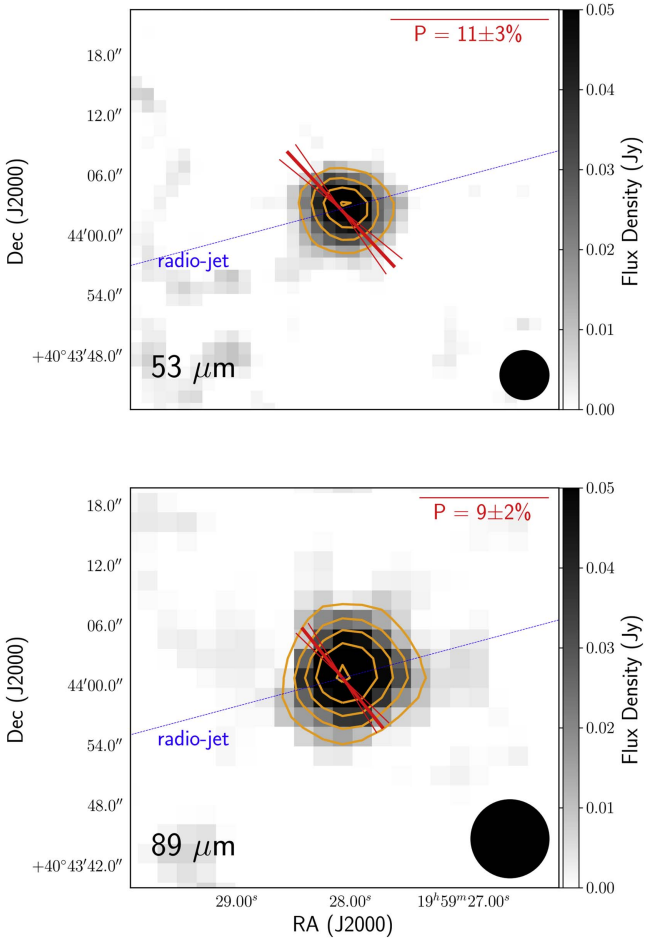

Figure 1. Imaging polarimetric observations at 53 (top) and 89 μm (bottom). Flux (grayscale) and polarization (red vector) with the uncertainty (thin red solid vector) in the PA of polarization within the beam size (black circles) are shown. Orange contours start at 3σ and increases in steps of 3σ. Radio-jet axis (blue dashed line) with a P.A.$_{\rm jet} \sim 284°$ (Sorathia et al. 1996) is shown.

Figure 1 shows the imaging polarimetric observations at 53 and 89 μm. In both bands, we found a point-like source with a highly polarized (∼10%) core with a PA of polarization of ∼40° (Table 1). To increase the signal-to-noise ratio (S/N) of the polarimetric measurements, we measure the nuclear polarization within the beam size at each band. These measurements provide a single statistically significant polarization vector at the ∼4σ level in the degree of polarization.

3. Nuclear Spectral Energy Distribution (SED)

We compile the total and polarized nuclear SED of Cygnus A with the best spatial resolution available from 2 μm to sub-mm wavelengths. Figure 2 (Table 1 in Appendix A) summarizes the data. For all observations, the angular resolution is below the separation of ∼45″ between the core and radio lobes, which ensures that the core is isolated from the radio lobes.

Table 1
Total and Polarized Nuclear Measurements of Cygnus A

λ (μm)	Aperture ($''$)	Flux Density (mJy)	P (%)	PA (°)	Polarized Flux (mJy)	References
2.0	0.375 (375 pc)	0.005 ± 0.001	10 ± 1.5	201 ± 3	0.49 ± 0.04	Tadhunter et al. (2000)
8.7	0.38 (380 pc)	29 ± 6	11 ± 3	27 ± 8	3.19 ± 0.66	Lopez-Rodriguez et al. (2014)
11.6	0.38 (380 pc)	45 ± 9	12 ± 3	35 ± 8	5.4 ± 2.08	Lopez-Rodriguez et al. (2014)
18.0	2.0 (2 kpc)	319 ± 27	...	...	...	Radomski et al. (2002)
53	5.0 (5 kpc)	2218 ± 222	11 ± 3	43 ± 8	244 ± 98	This work (HAWC+)
70	6 (6 kpc)	2520 ± 30	...	...	...	This work (*Herschel*)
89	8.0 (8 kpc)	2088 ± 195	9 ± 2	39 ± 7	188 ± 63	This work (HAWC+)
100	7 (7 kpc)	2160 ± 10	...	...	...	This work (*Herschel*)
160	12 (12 kpc)	1260 ± 20	...	...	...	This work (*Herschel*)
250	21 (21 kpc)	560 ± 40	...	...	...	This work (*Herschel*)
350	29 (29 kpc)	390 ± 90	...	...	...	This work (*Herschel*)
500	41(41 kpc)	360 ± 110	...	...	...	This work (*Herschel*)
1303	1.0 (1.0 kpc)	480 ± 48	...	...	...	Wright & Birkinshaw (2004)
1400	12 (12 kpc)	...	null	...	<3.9	Ritacco et al. (2017)
2000	18.2 (18.2 kpc)	...	null	...	<1.5	Ritacco et al. (2017)
3446	1.0 (1.0 kpc)	1050 ± 105	...	...	...	Wright & Birkinshaw (2004)
19986	1.0 (1.0 kpc)	1350 ± 135	...	...	...	Wright & Birkinshaw (2004)
59958	1.0 (1.0 kpc)	880 ± 88	...	...	...	Wright & Birkinshaw (2004)

3.1. Total Flux SED

We took *Herschel* observations of Cygnus A from the *Herschel* Archive.[6] To our knowledge, these data have not been published before, so we present the observations here. At all wavelengths, the core and radio lobes are resolved, which allows us to perform photometric measurements of the core without any contamination from the radio lobes. We found that the flux density of the core decreases with increasing wavelength, while the flux density of the radio lobes increases (Figure 3). We did not find any contribution from the lobes in our 53 and 89 μm HAWC+ observations, which indicates that the nuclear photometric and polarimetric measurements are dominated by a compact unresolved component.

Observationally, we find that the nuclear SED of Cygnus A shows a turnover emission in the mm wavelength regime, and an IR bump peaking at ∼40 μm. We fitted a model to the SED (Figure 2, top-left panel). We find that a self-absorbed synchrotron component with a flat spectrum ($F_\nu \propto \nu^{\alpha_{\rm tk}}$, with $\alpha_{\rm tk} = +0.21 \pm 0.05$) in the optically thick region with a turnover at $\nu_c = 552 \pm 100$ GHz ($\lambda_c = 543 \pm 120$ μm) best explains the mm range. The index of the optically thin region ($\alpha_{\rm th} = -1.9 \pm 1.1$) cannot be well constrained due to the contribution of the IR bump. The synchrotron emission is insignificant at IR wavelengths in the core of Cygnus A.

The IR bump is best described by a single blackbody component from 10 to 500 μm. Then, a torus component is required to account for the 10 μm silicate feature, and starlight is required to account for the emission at 2 μm. We use the CLUMPY torus template for the archetypical Type 2 AGN, NGC 1068, inferred using subarcsecond angular resolution observations from IR to sub-mm wavelengths (Lopez-Rodriguez et al. 2018b). For the starlight component, we use the Elliptical galaxy template from the *Spitzer* Wide-area InfraRed Extragalactic survey (SWIRE) template library[7] (Polletta et al. 2007). The blackbody component has a characteristic color temperature of 107 ± 9 K, assuming a dust emissivity of $\nu^{1.6}$. Our color temperature is compatible with the estimated dust temperature of 150 ± 10 K within the central 2 kpc using N-band observations using OSCIR/Keck II (Radomski et al. 2002). For Cygnus A, Kafatos et al. (1980) suggested a non-thermal origin up to sub-mm wavelengths with a thermal component as the dominant components at IR wavelengths, which agrees with our well-sampled nuclear SED. These results agree with the spectra of lobe-dominant quasars having a non-thermal component with a turnover in the sub-mm wavelength range and an IR excess (Antonucci et al. 1990).

Our SED fitting shows that a single blackbody component does not account for both the 10 μm window and 2 μm measurements. We explain the emission in the 10 μm window as the mixture of contributions from the dust emission of the blackbody component and the pc-scale CLUMPY torus. Merlo et al. (2014) found that the 10 μm silicate absorption feature observed using the Cooled Mid-Infrared Camera and Spectrometer (COMICS)/Subaru can be explained by a blackbody component with a temperature of 217 ± 3 K obscured by cold dust with a characteristic temperature of <50 K, or a CLUMPY. We explain the emission at 2 μm as dominated by starlight/scattered light (Section 3.2).

Using the estimated blackbody temperature of 107 ± 9 K, and the bolometric luminosity of 1×10^{45} erg s^{-1} (Radomski et al. 2002), we estimated an extension of the dust emission to be within a radius of 17 ± 3 pc (∼17 mas). Imanishi & Ueno (2000) suggested an obscuring dusty structure with inner radius of 2.25 pc and outer radius of a few hundred pc based on IR SED fitting. We estimate the dust mass at the peak frequency from a modified blackbody using, in practical units, $M_d = 1.6 \times 10^{-6} \nu_{1000\,\rm GHz}^{-(2+\beta)} S_{\nu,\rm Jy} T_{d,K}^{-1} D_{\rm pc}\, M_\odot$ (Berta et al. 2016), where $\nu_{1000\,\rm GHz}$ is the frequency normalized to 1000 GHz, β is the index of the dust opacity, $T_{d,K}$ is the dust temperature of the blackbody component in units of K, and $D_{\rm pc}$ is the distance to the source in units of pc. We took $\nu_{1000\,\rm GHz} = 2.99$, $\beta = 1.6$, $T_{d,K} = 107 \pm 9$ K, and $D_{\rm pc} = 2.37 \times 10^8$ Mpc, and estimate a dust mass of $M_d = 3.3 \pm 0.6 \times 10^7\, M_\odot$. Young et al. (2002) estimated a column density of gas to be $N_H = 2 \times 10^{23}$ cm^{-2} using X-ray *Chandra* observations. We took this column

[6] *Herschel* Archive can be found at http://archives.esac.esa.int/hsa/whsa/.
[7] The SWIRE template library can be found at http://www.iasf-milano.inaf.it/~polletta/templates/swire_templates.html.

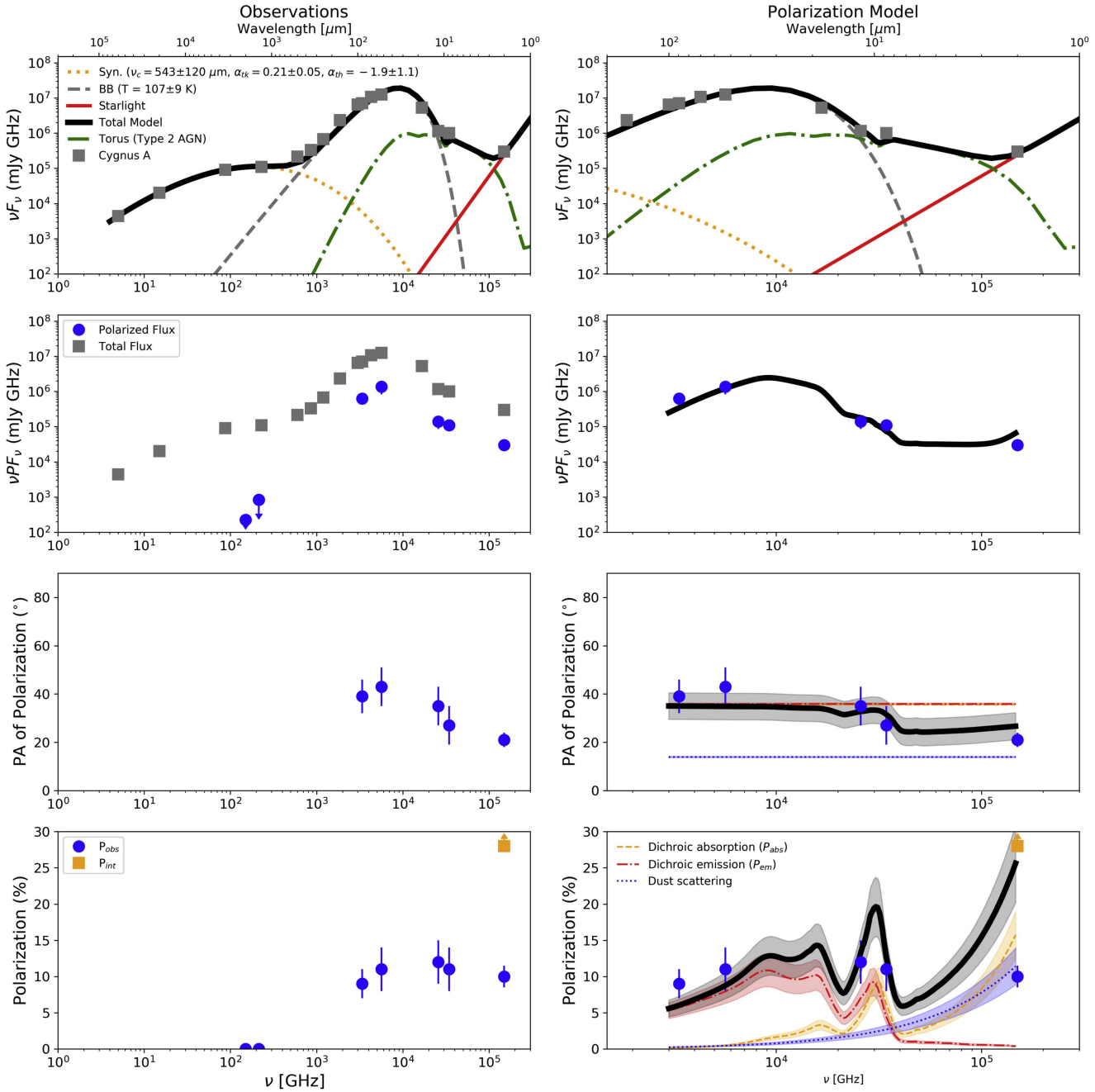

Figure 2. Observations (left column) and polarization model (right column) of the nucleus of Cygnus A showing the total (first row) and polarized (second row) fluxes, PA (third row), and degree (fourth row) of polarization. The intrinsic (starlight-corrected) nuclear polarization (orange square) at 2.2 μm by Tadhunter et al. (2000) is shown. SED model: a self-absorbed synchrotron component (orange dotted line), a blackbody component with color temperature of 107 ± 9 K (gray dashed line), a clumpy torus model of a Type 2 AGN (green dashed line), and a starlight component (red solid line) describe the nuclear SED of Cygnus A. Polarized SED model: the combination of dichroic absorption (orange) and emission (red), and dust scattering (blue) explain the degree and PA of polarization. The total polarized flux model (black line) is estimated as the multiplication of the total flux model by the total polarization model.

density and estimated a gas mass of $3 \times 10^8\,M_\odot$ within a 17 pc radius (Wilman et al. 2000, Equation (2)). We finally estimated the gas-to-dust ratio to be 0.1. Using a sample of 48 galaxies in the Spitzer Infrared Nearby Galaxies Survey (SINGS) sample, Draine et al. (2007) found a dust-to-gas ratio in the range of 0.002–0.005. Parkin et al. (2012) estimated a dependence of the dust-to-gas ratio as a function of the distance to the central source of Centaurus A with an average of 0.001 in an area of 10×2 arcmin^2. Typical Galactic values of the gas-to-dust ratio varies from 0.006 to 0.008 (e.g., Li & Draine 2001; Zubko et al. 2004).

3.2. Nuclear Polarization

Ritacco et al. (2017) performed 12″ and 18.″2 resolution polarimetric observations at 1.15 and 2.05 mm of Cygnus A. They found an unpolarized core, with highly polarized, ∼10%, radio lobes with perpendicular PA of polarization to each other. Using their observations, we obtain a 3σ upper-limit of the polarized flux of the core to be <3.9 and <1.5 mJy at 1.15 and 2.05 mm, respectively. We measured the polarization of Cygnus A to be 0.4% to 3.2% with a fairly constant PA of polarization of ∼165° from 30 to 217 GHz using *Planck*

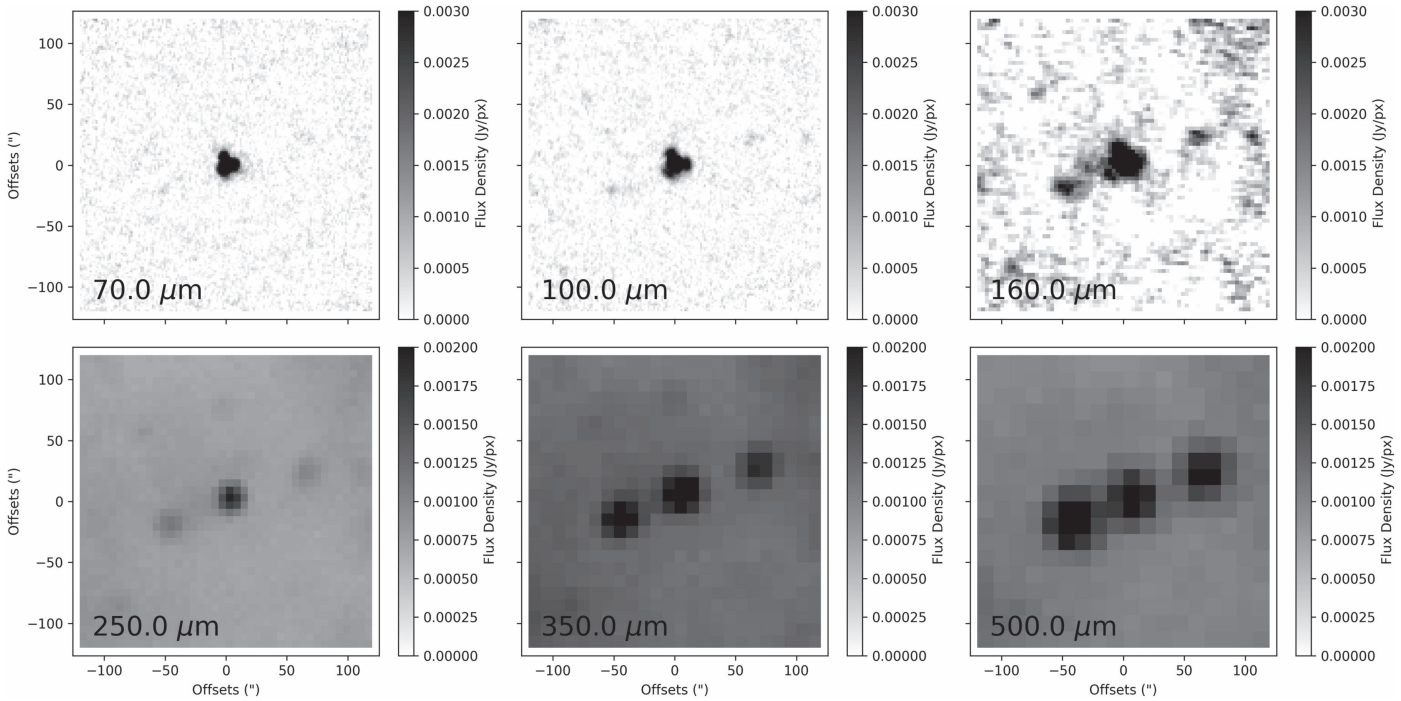

Figure 3. *Herschel* images of Cygnus A at 70, 100, 160, 250, 350, and 500 μm obtained with Photodetector Array Camera and Spectrometer (PACS) and the Spectral and Photometric Imaging REceiver (SPIRE). The field of view is 40 × 40 (240 × 240 kpc^2).

observations (Planck Collaboration et al. 2016), in a 5′ aperture at 545 GHz and a 30′ aperture at 30 GHz. The low angular resolution from *Planck* measurements are highly affected by the polarized radio lobes, and they are not used in this Letter.

Observationally, we find the polarized SED (Figure 2, top-right panel) has the same shape as the IR bump of the total flux SED. Despite the angular resolution observations from 2.0 to 89 μm, the degree of polarization remains nearly constant ($\sim$10%) within the uncertainties, although a tentative decrease in the degree of polarization from 10 to 89 μm is observed. We measure a statistically significant change of $\sim$20° in the PA of polarization from 2 to 89 μm. The change in the PA of polarization from 2 to 89 μm, and the tentative change of the degree polarization in the 10–89 μm indicate a change of polarization mechanisms between 2 and 89 μm.

We investigate the several polarization mechanisms arising from the nucleus of Cygnus A from 1 to 100 μm. Specifically, we follow similar techniques as presented by Aitken et al. (2004) and Lopez-Rodriguez (2016), which have been proven (e.g., Smith et al. 2000) to be useful to disentangle the several competing polarization mechanisms in the MIR. We here extend this polarization technique to the wavelength range from 1 to 100 μm. The known polarization profiles of the absorptive and emissive polarization components, as well as the wavelength-dependent cross-section dust scattering within the 1–100 um, are linearly combined to obtain the best fit to the normalized Stokes *qu*. Specific details are shown in Appendix B. As shown in Section 3.1, synchrotron emission is insignificant in the IR, therefore this component is not used in the polarization model. The right panels of Figure 2 show the final polarization model for the total and polarized flux, and for the degree and PA of polarization. Figure 4 shows polarization profiles, and best fit to the normalized Stokes *qu*.

Our best fit shows that the combination of dichroism and dust scattering best explain the wavelength-dependent degree and PA of polarization in the 1–100 μm wavelength range. Figure 4 shows the fractional contribution of each polarization mechanism per wavelength. We find that the 20–100 μm polarized SED is explained by dichroic emission of aligned dust grains in the unresolved core of Cygnus A. Polarization arising by dichroic emission is the dominant polarization mechanism in the 20–100 μm wavelength range. In the 8–12 μm wavelength range, dichroic emission and dichroic absorption compete. This behavior has been found to be typical in astrophysical objects, i.e., star-forming regions, young stellar objects, etc. (Smith et al. 2000). At 2 μm, dust scattering polarization is extinguished by the dichroic absorption component, both having statistically significant different PAs of polarization of 36° ± 6° and 14° ± 5°, respectively. In a sample of 13 FRII galaxies, Ramírez et al. (2014) found that dichroic absorption as well as scattering can be the dominant polarization mechanisms at 2 μm, but the single wavelength polarization observation made it difficult to disentangle them. The polarization at 2 μm is interpreted as a combination of several mechanisms, i.e., dust scattering and dichroic absorption. We note that our estimated PA of polarization of 14° ± 5° at 2 μm arising from dust scattering is perpendicular to the radio jet axis of P.A.$_{\rm jet}$ $\sim$ 284° (Sorathia et al. 1996).

4. Final Remarks

As mentioned in the introduction, the UV/optical polarization (Tadhunter et al. 1990, 2000; Ogle et al. 1997; Hurt et al. 1999; van Bemmel et al. 2003) is dominated by dust scattering arising from the few-kpc-scale bicone. No information about the core is obtained due to the obscured core at these wavelengths. The fact that the PA of polarization remains perpendicular to the jet direction from UV to 2 μm (Packham et al. 1998; Tadhunter et al. 2000; Ramírez et al. 2014) and considering the results from our polarization model, we suggest that the 2 μm polarization arises from dust scattering from an

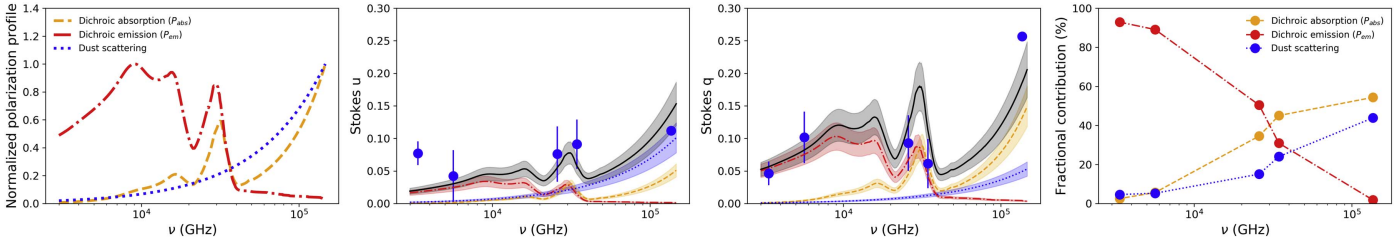

Figure 4. Normalized polarization profiles of the absorptive (orange dashed line), emissive (red dotted–dashed line) and dust scattering (blue dotted line) components used to fit the observed Stokes *qu* of the nuclear polarization of Cygnus A in Figure 2. Fractional contribution (fourth panel) of the polarization mechanisms on our observations.

unresolved dusty scattering region within the 350 pc central region. The dichroic absorption component of our model indicates the need of extinction correction to obtain the intrinsic polarization at 2 μm. The change in the PA of polarization of $\sim$20° from 2 to 89 μm suggests a change of polarization mechanisms.

The nearly constant PA of polarization in the FIR, the near-perfect match between the total and polarized SED at wavelengths >2 μm, the estimated high dust-to-gas ratio at 17 pc using the blackbody component with color temperatures of 107 ± 9 K, and our polarization model all indicate that dichroic dust emission becomes dominant at FIR wavelengths. It also suggests a fairly coherent and well-defined, albeit unresolved, structure for this emitting dust. The MIR polarization seems to be in the wavelength range where the transition of polarization mechanisms take place. Specifically, the MIR polarization arises from a contribution of absorptive and emissive polarization from aligned dust grains surrounding the AGN. We note that previous analysis (Lopez-Rodriguez et al. 2014) has suggested that the dominant MIR polarization arises from polarized synchrotron emission from the pc-scale jet of Cygnus A. Although their suggested power law with a cutoff at $\sim$34 μm agrees with our blackbody component explaining the IR bump, their interpretation was biased due to the lack of available FIR and sub-mm polarimetric observations. Thus, we here stress the need of FIR and sub-mm polarimetric observations to investigate the cores of AGN.

We compare our measured polarization and suggested interpretation with other AGN and astrophysical objects in the 10–100 μm wavelength range. Siebenmorgen & Efstathiou (2001) and Lopez-Rodriguez et al. (2018a) found several highly polarized, 2%–8%, AGN in the 7–14 μm wavelength range using the *Infrared Space Observatory* and the GTC, respectively. At these wavelengths, AGN cores are known to be unpolarized, while high polarization arises from diffuse extended emission (Lopez-Rodriguez et al. 2018a). Polarization up to $\sim$12% at 60–110 μm using the Kuiper Airborne Observatory have been found around star-forming regions (i.e., OMC1 and W3) and the Galactic center radio arc (i.e., Novak et al. 1997; Dotson et al. 2000). Theoretical models (e.g., Hildebrand et al. 2000; Aitken et al. 2002; Vaillancourt 2002) show that the FIR polarization arises from emission of aligned dust grains with several magnetic field configurations. These results support the theory that the observed high polarized Cygnus A core within the 10–100 μm arises from aligned dust grain emission. Further FIR polarimetric and deeper observations of a larger AGN sample and wavelength coverage will provide statistically significant results to investigate how ordinary or extraordinary these findings are and to study the role of the magnetic field configuration.

We are grateful to Chris Packham and Edgar Ramirez for their numerous comments that helped to clarify and improve the text. Based on observations made with the NASA/DLR Stratospheric Observatory for Infrared Astronomy (SOFIA). SOFIA is jointly operated by the Universities Space Research Association, Inc. (USRA), under NASA contract NAS2-97001, and the Deutsches SOFIA Institut (DSI) under DLR contract 50 OK 0901 to the University of Stuttgart. Financial support for this work was provided by NASA through award #05_0071 issued by USRA. *Herschel* is an ESA space observatory with science instruments provided by European-led Principal Investigator consortia and with important participation from NASA. E.L.-R. acknowledges support from the Japanese Society for the Promotion of Science (JSPS) through award PE17783, the National Observatory of Japan (NAOJ) at Mitaka and the Thirty Meter Telescope (TMT) Office at NAOJ-Mitaka for providing a space to work and great collaborations during the short stay in Japan.

Facilities: SOFIA (HAWC+), *Herschel* (PACS, SPIRE).

Software: astropy (Astropy Collaboration et al. 2013).

Appendix A
Supporting Material

Table 1 shows the total and polarized measurements of the nucleus of Cygnus A used in Section 3. Figure 4 shows the *Herschel* images of Cygnus A.

Appendix B
Polarization Model

Normalized Stokes *qu* are linear combinations of the dichroic absorption, emission, and dust scattering profiles, such as:

$$\begin{aligned} q(\lambda) &= A f_{\rm abs}(\lambda) + B f_{\rm em}(\lambda) + C f_{\rm sca}(\lambda) \\ u(\lambda) &= D f_{\rm abs}(\lambda) + E f_{\rm em}(\lambda) + F f_{\rm sca}(\lambda) \end{aligned} \quad (1)$$

where A, B, C, D, E, and F are scaling factors of the normalized absorptive, $f_{\rm abs}(\lambda)$, emissive, $f_{\rm abs}(\lambda)$ and dust scattering, $f_{\rm sca}(\lambda)$, and polarization components that need to be estimated through a fitting routine. We used the fitting routine described by Lopez-Rodriguez (2016), and set the scaling factors as uniform priors within the range of -0.3 to 0.3 of the normalized Stokes *qu*. Degree and PA of polarization are estimated as $P = \sqrt{q(\lambda)^2 + u(\lambda)^2}$, and P.A. $= 0.5 \times \arctan(u(\lambda)/q(\lambda))$, respectively.

Polarization profiles were taken[8] from the carbonaceous—silicate model for interstellar dust (Weingartner & Draine 2001).

[8] The extinction curves can be found at https://www.astro.princeton.edu/~draine/dust/dustmix.html.

The typical Galactic extinction of $R_V = 5.5$ was used. Given the uncertainties of our observations, we find little difference between the several values of R_V in our final model. The absorptive polarization, $P_{\rm abs}$, is the combination of a Serkowski curve (Serkowski et al. 1975) up to 5 μm, then the extinction curve, τ_λ, is used. The emissive profile is estimated as $P_{\rm em} = P_{\rm abs}/\tau_\lambda$. For the dust scattering profile, the wavelength-dependent cross-scattering sections for this model were used. The best values of the scaling factors are $A = 0.053 \pm 0.011$, $B = 0.047 \pm 0.010$, $C = 0.187 \pm 0.041$, $D = 0.103 \pm 0.022$, $E = 0.095 \pm 0.021$, and $F = 0.103 \pm 0.022$.

ORCID iDs

Enrique Lopez-Rodriguez https://orcid.org/0000-0001-5357-6538
Ranga-Ram Chary https://orcid.org/0000-0001-7583-0621
Makoto Kishimoto https://orcid.org/0000-0002-2216-3252

References

Aitken, D. K., Efstathiou, A., McCall, A., & Hough, J. H. 2002, MNRAS, 329, 647
Aitken, D. K., Hough, J. H., Roche, P. F., Smith, C. H., & Wright, C. M. 2004, MNRAS, 348, 279
Antonucci, R. 1993, ARA&A, 31, 473
Antonucci, R., & Barvainis, R. 1990, ApJL, 363, L17
Antonucci, R., Barvainis, R., & Alloin, D. 1990, ApJ, 353, 416
Astropy Collaboration, Robitaille, T. P., Tollerud, E. J., et al. 2013, A&A, 558, A33
Berta, S., Lutz, D., Genzel, R., Förster-Schreiber, N. M., & Tacconi, L. J. 2016, A&A, 587, A73
Dotson, J. L., Davidson, J., Dowell, C. D., Schleuning, D. A., & Hildebrand, R. H. 2000, ApJS, 128, 335
Draine, B. T., Dale, D. A., Bendo, G., et al. 2007, ApJ, 663, 866
Harper, D. A., Runyan, M. C., Dowell, C. D., et al. 2018, JAI, submitted
Hildebrand, R. H., Davidson, J. A., Dotson, J. L., et al. 2000, PASP, 112, 1215
Hurt, T., Antonucci, R., Cohen, R., Kinney, A., & Krolik, J. 1999, ApJ, 514, 579
Imanishi, M., & Ueno, S. 2000, ApJ, 535, 626
Kafatos, M., Maran, S. P., Brown, L. W., & Hobbs, R. W. 1980, ApJ, 235, 18
Koljonen, K. I. I., Russell, D. M., Fernández-Ontiveros, J. A., et al. 2015, ApJ, 814, 139
Li, A., & Draine, B. T. 2001, ApJ, 554, 778
Lopez-Rodriguez, E. 2016, MNRAS, 455, 2656
Lopez-Rodriguez, E., Alonso-Herrero, A., Diaz-Santos, T., et al. 2018a, MNRAS, 478, 2350
Lopez-Rodriguez, E., Fuller, L., Alonso-Herrero, A., et al. 2018b, ApJ, 859, 99
Lopez-Rodriguez, E., Packham, C., Tadhunter, C., et al. 2014, ApJ, 793, 81
Merlo, M. J., Perlman, E. S., Nikutta, R., et al. 2014, ApJ, 788, 6
Novak, G., Dotson, J. L., Dowell, C. D., et al. 1997, ApJ, 487, 320
Ogle, P. M., Cohen, M. H., Miller, J. S., et al. 1997, ApJL, 482, L37
Packham, C., Young, S., Hough, J. H., Tadhunter, C. N., & Axon, D. J. 1998, MNRAS, 297, 936
Parkin, T. J., Wilson, C. D., Foyle, K., et al. 2012, MNRAS, 422, 2291
Planck Collaboration, Ade, P. A. R., Aghanim, N., et al. 2016, A&A, 594, A26
Polletta, M., Tajer, M., Maraschi, L., et al. 2007, ApJ, 663, 81
Privon, G. C., Baum, S. A., O'Dea, C. P., et al. 2012, ApJ, 747, 46
Radomski, J. T., Piña, R. K., Packham, C., Telesco, C. M., & Tadhunter, C. N. 2002, ApJ, 566, 675
Ramírez, E. A., Tadhunter, C. N., Axon, D., et al. 2014, MNRAS, 444, 466
Ritacco, A., Ponthieu, N., Catalano, A., et al. 2017, A&A, 599, A34
Serkowski, K., Mathewson, D. S., & Ford, V. L. 1975, ApJ, 196, 261
Siebenmorgen, R., & Efstathiou, A. 2001, A&A, 376, L35
Smith, C. H., Wright, C. M., Aitken, D. K., Roche, P. F., & Hough, J. H. 2000, MNRAS, 312, 327
Sorathia, B., Bartel, N., Beitenholz, M., & Carilli, C. 1996, in The Parsec-scale Jet and Counterjet in Cygnus A, ed. C. L. Carilli & D. E. Harris (Cambridge: Cambridge Univ. Press), 86
Stockton, A., Ridgway, S. E., & Lilly, S. J. 1994, AJ, 108, 414
Tadhunter, C. N., Scarrott, S. M., & Rolph, C. D. 1990, MNRAS, 246, 163
Tadhunter, C. N., Sparks, W., Axon, D. J., et al. 2000, MNRAS, 313, L52
Urry, C. M., & Padovani, P. 1995, PASP, 107, 803
Vaillancourt, J. E. 2002, ApJS, 142, 53
Vaillancourt, J. E., Chuss, D. T., Crutcher, R. M., et al. 2007, Proc. SPIE, 6678, 66780D
van Bemmel, I. M., Vernet, J., Fosbury, R. A. E., & Lamers, H. J. G. L. M. 2003, MNRAS, 345, L13
Weingartner, J. C., & Draine, B. T. 2001, ApJ, 548, 296
Wilman, R. J., Edge, A. C., Johnstone, R. M., Crawford, C. S., & Fabian, A. C. 2000, MNRAS, 318, 1232
Wright, M. C. H., & Birkinshaw, M. 2004, ApJ, 614, 115
Young, A. J., Wilson, A. S., Terashima, Y., Arnaud, K. A., & Smith, D. A. 2002, ApJ, 564, 176
Zubko, V., Dwek, E., & Arendt, R. G. 2004, ApJS, 152, 211